Intermetallics 50 (2014) 65–78

Contents lists available at ScienceDirect

Intermetallics

journal homepage: www.elsevier.com/locate/intermet

Characterization of microstructures and age hardening of $Fe_{1-2x}Al_xV_x$ alloys

P.A. Ferreirós [a], P.R. Alonso [a], P.H. Gargano [a], P.B. Bozzano [a], H.E. Troiani [b,c], A. Baruj [b,c], G.H. Rubiolo [a,b,*]

[a] Gerencia de Materiales (GAEN) – Comisión Nacional de Energía Atómica (CNEA), Instituto Sabato – Universidad Nacional de San Martín (UNSAM), Av. Gral. Paz 1499, San Martín, Buenos Aires B1650KNA, Argentina
[b] Consejo Nacional de Investigaciones Científicas y Técnicas (CONICET), Av. Rivadavia 1917, C1033AAJ Ciudad Autónoma de Buenos Aires, Argentina
[c] Centro Atómico Bariloche (CNEA) and Instituto Balseiro (UNCuyo/CNEA), Av. Ezequiel Bustillo 9500, S. C. de Bariloche, Río Negro, Argentina

ARTICLE INFO

Article history:
Received 16 September 2013
Received in revised form
4 February 2014
Accepted 20 February 2014
Available online 14 March 2014

Keywords:
A. Iron aluminides (based on Fe3Al)
B. Alloy design
B. Age-hardening
E. ab-initio calculations
F. Calorimetry
F. Electron microscopy, transmission

ABSTRACT

The Fe-rich corner of the Fe–Al–V system has shown phase separation into disordered A2 and ordered $L2_1$ phases. In a former work we model this ordering reaction by using ab-initio thermodynamics. The approach is now employed to suggest the $Fe_{1-2x}Al_xV_x$ alloys in order to reduce the Al content by increasing the addition of vanadium looking for a better ductility of the solid solution which can be afterwards strengthened by coherent $L2_1$ precipitates. Four alloys with compositions in the range $0.08 < X < 0.15$ were studied. The phase transition temperatures and microstructures of the alloys were characterized by differential scanning calorimetry (DSC) and transmission electron microscopy (TEM), respectively. The region (A2 + $L2_1$) occurs for $0.10 < X < 0.15$ up to maximum temperature of 720 °C, higher temperatures causes the appearance of (A2 + B2), B2 and (B2 + $L2_1$) regions. The microstructure in the (A2 + $L2_1$) region consists of nanosized precipitates of $L2_1$ phase in A2 matrix which morphology evolutes with temperature and ageing time. The hardness values, measured at room temperature, for the alloys with $X < 0.125$ and ageing temperature between 650 and 700 °C are comparable to those obtained with other Fe–Al based alloys.

1. Introduction

The development of Fe–Al alloys for applications as structural materials at high temperature, in oxidizing or reducing environments, has employed considerable research work over the past several decades [1–6]. Due to the low creep strength of binary Fe–Al alloys above 600 °C [7], much of this effort was focused on improving this property by alloying with titanium, niobium, molybdenum, zirconium, hafnium, boron, carbon and obtaining a large volume fractions of second phases, often brittle intermetallic phases [8–16]. However, this approach often has left the material with high brittle–ductile transition temperature even when the creep temperature goal was reached [8–13,16]. The strengthening by coherent particles was less attempted. Fe_2AlX (X = Ti, V, Nb, Ta) type phase with the $L2_1$ (Heusler) structure is known to form coherent precipitates in a body-centered cubic (BCC) α-(Fe, Al) disordered matrix [17–20]. Thus, Fe–Al-based A2/$L2_1$ alloys should be microstructurally analogous to classical Ni–Al-based A1/$L1_2$ superalloys. However, very often the precipitation of the Heusler-type phase occurs together with the precipitation of a incoherent $(Fe, Al)_2$ X type phase with the hexagonal C14 (Laves) structure. The precipitation of the Laves phase is unavoidable in the Fe–Al–Nb and Fe–Al–Ta systems [3,21] while the Fe–Al–Ti system offers a certain range of composition and temperatures where that precipitation can be suppressed [22]. Because the binary Fe–V system shows only the FeV phase with the D8b (sigma) structure and is known that the solid solubility of Al in this phase is very limited [23], it is expected that the precipitation of the Heusler-type phase not be screened by any other. In fact, Maebashi et al. [24] has reported phase separation into disordered A2 and ordered $L2_1$ phases in a wide composition range in the Fe-rich corner of Fe–Al–V system at 923 K, 973 K and 1023 K in absence of any other phase.

The alloy Fe–23Al–8.5Ti [25] with coherent A2/$L2_1$ microstructure has shown at 650 °C a flow stress of 650 MPa and a creep

* Corresponding author. Present address: Gerencia de Materiales, Departamento de Transformaciones y Propiedades, Comisión Nacional de Energía Atómica, Avda Gral Paz 1499, B1650KNA San Martín, Argentina. Tel.: +54 11 6772 7240; fax: +54 11 6772 7362.
E-mail address: rubiolo@cnea.gov.ar (G.H. Rubiolo).

http://dx.doi.org/10.1016/j.intermet.2014.02.014
0966-9795/

resistance of 240 MPa for a secondary creep rate of 10^{-7} s^{-1}. Exposure to higher temperatures leads to a deterioration of these mechanical properties because the $L2_1$ phase coarsened and lost coherency with the A2 matrix. Compared to binary Fe–Al alloys these results are remarkably good but, its brittle-to-ductile transition temperature (BDTT) is around 925 °C and may, at least in the moment, preclude their application at 650 °C as the alloys will fail in a brittle manner in case of any damage.

In two-phase materials, such as Fe–Al-based A2/$L2_1$ alloys, it is expected that many properties will be closely related to the intrinsic properties of these two phases. The effects of Al, Ti and V on the ductility and toughness of the α-Fe phase have been reported in literature. Specifically, the strongest effect is produced by Al where the BDTT increases from −110 °C up to 140 °C when the Al content increases to 18 at.% [26], also Ti increases the BDTT up to 0 °C for an increment of 3.5 at.% [27], while V tends to reduce the BDTT in the range from 0 to 9 at.% and then raise 6 °C per atomic percent up to 16 at.% [28]. At higher Al contents above 20 at.%, $D0_3$ atomic ordering occurs in the binary Fe–Al alloys but the results do not indicate any effect of atomic ordering on the BDTT, i.e. the BDTT remains unchanged from 19.8 to 25.8 at.% Al followed by a slight decrease between 25.8 and 29 at.% Al [29]. The addition of titanium or vanadium to the $D0_3$ structure stabilizes the $L2_1$ structure, its ternary equivalent, so the $L2_1$-B2 transformation reaches values as high as 1000 °C and above [30,31]. This stabilization has consequence on the BDTT as measured by the addition of Ti where was find to increase up values ranging between 750 and 850 °C. In the authors' knowledge there is no work published concerning the effect of vanadium addition on the BDTT of the $L2_1$ structure however, the substitution of Ti and V correlates well pushing to higher temperatures the anomalous yield stress peak in parallel with the increase in the $D0_3$-B2 transformation temperature [32] therefore, it can be expected that the addition of vanadium rises the BDTT in the same way as titanium.

Based on the available literature, it is implicit that the dissolved Al and thirds elements in the α-Fe solid solution, the solvus temperature of this solid solution, and the volume fraction and stoichiometry of the coherent particles are expected to be the major factors controlling the strength and ductility of these coherent two-phase alloys. In this sense the Fe-rich corner of the Fe–Al–V system has been less explored, inspection of the results in Ref. [24] shows that the solvus composition may be chosen to reduce the Al content by increasing the addition of vanadium and both factors contribute to the ductility but there is at least three initials unknowns to respond: the maximum temperature for the (A2 + $L2_1$) field, the volume fraction of coherent phase for each composition in the maximum temperature and the hardening power of the coherent precipitation. The present study attempts to answer these three questions for the alloys $Fe_{1-2x}Al_xV_x$, the choice of this composition relationship is also discussed. The deformation behavior at high temperatures as well as the evaluation of BDTT will be subjects of a future work.

2. Alloy design

In a former work [33] we model the BCC phase diagrams of the technologically important systems Fe–Al–X (X = Ti, Nb, V) by using ab-initio thermodynamics. There was concluded that the Fe–Al–V system display two kinds of phase separations of the BCC phase, (A2 + $L2_1$) and (B2 + $L2_1$), separate by a tie-line. As the temperature increases this tie-line shrinks and moves toward the Fe–V binary system while its direction remains almost parallel. Vertical sections of the ternary phase diagrams containing this tie-line can be used to design alloys where only two-phase A2 + $L2_1$ coherent microstructures can be generated.

Fig. 1 display the overlapping isothermal sections of the ternary Fe–Al–V equilibrium diagram obtained by the calculations with the data of reference [33], there is observed that the border tie-line between both biphasic fields (A2 + $L2_1$) and (B2 + $L2_1$) is held nearly parallel at various temperatures and this direction is parallel to the line from pure iron to the compound Fe_2AlV. So, any vertical section of the ternary diagram parallel to the section containing the line $Fe_{1-2x}Al_xV_x$ will show the border tie-line parallel to the composition axe. Going from aluminum-rich sections to that of the same composition in aluminum and vanadium, the temperature of the border tie-line increases and the two-phase (A2 + $L2_1$) coherent microstructures could be generated at higher temperatures and with less aluminum content. In order to preserve the idea of designing a Fe–Al based alloy strengthened by coherent particles and good ductility at low temperature, we chose the limit section $Fe_{1-2x}Al_xV_x$ for the selection of alloys to be investigated.

Fig. 2(a) shows the experimental data of Ref. [24] in the $Fe_{1-2x}Al_xV_x$ section together with our ab-initio calculations. This comparison attempts to display the topological differences between them since, as reported previously by many authors (for instance [34], and references therein), ab-initio calculations overestimate the temperature scale but give good results in the modeling of qualitative features of the experimental phase diagram. Thus, the comparison allows us to guess that a single phase field B2 and a biphasic field (B2 + $L2_1$) may be expected at high temperatures in the experimental phase diagram as is hypothetically shown in Fig. 2(b). These fields are not reported in Ref. [24] although homogenization treatments were performed at 1350 °C. In order to test this hypothesis, we design four alloys which nominal composition is drawn as vertical line in Fig. 2(b).

3. Experimental

The four alloy selected for the present study were fabricated by vacuum arc melting from high purity Fe (99.97 wt. %), Al (99.99 wt. %) and Ti (99.7 wt. %) to produce 12 g cast buttons. The buttons were wrapped in a Tantalum foil, encapsulated into a quartz tube which was evacuated and back-filled with argon and subjected to a homogenization treatment at 1100 °C for 136 h. All alloys were solution treated at 1100 °C for 2 h in a vertical drop furnace under flowing argon atmosphere followed by a water quench. The last procedure was also used to age the alloys, temperatures and times for ageing treatments are presented in the text following the discussion about their microstructure.

Samples for optical and scanning electron microscopy (SEM) were machined using electro discharge machining (EDM). The samples were mechanically polished to 1 μm grade diamond powder finish and etched using an etchant comprising 68% glycerine, 16% HF and 16% HNO3 by volume. Carbon extraction replicas were obtained by the classical method [35], a carbon film (estimated thickness of 15–30 nm) is evaporated on to the polished sample surface. The film is removed by chemical etching in a bath of 4% nitric acid in ethanol. Microstructural analysis was performed by using a PHILIPS Inspect F50 and the elemental compositions were obtained with Energy Dispersive Spectroscopy (EDS) in the same device. The average chemical compositions of the alloys were determined on homogenized samples with electron-probe microanalysis (EPMA) in Cameca SX50 equipment fitted with a wavelength-dispersive spectrometer.

All the transformation temperatures were determined from differential scanning calorimetric (DSC; Setaram LABSYS evo) measurements with heating rate of 10 °C/min under an argon flow of 25 mL/min, also higher speeds eventually were used. Samples for DSC testing were cut from homogenized alloys by EDM (cylinders of 3 mm in diameter and weight between 40 and 90 mg).

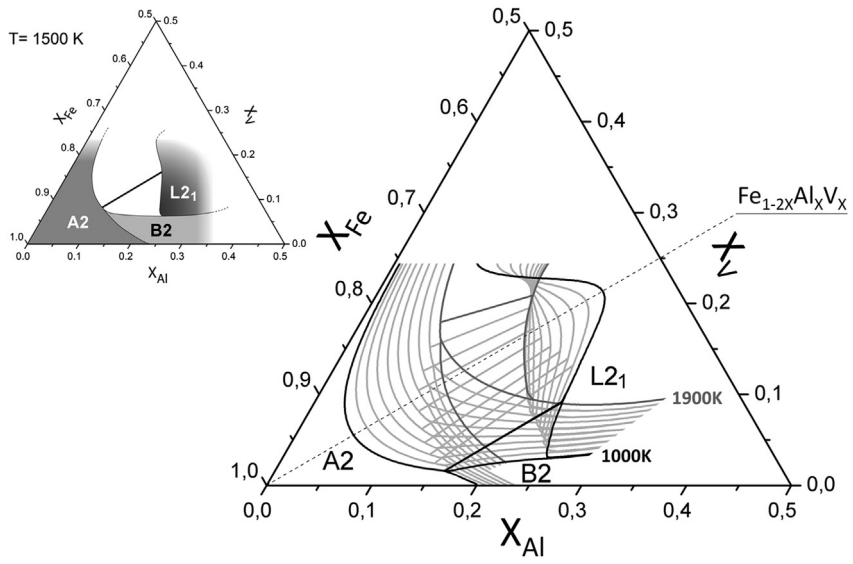

Fig. 1. Ab-initio thermodynamics modeling of Fe–Al–V ternary system. Overlapping of isothermal sections from 1000 to 1900 K. The dash dotted line indicates the composition $Fe_{1-2x}Al_xV_x$. The inset show one of these isotherms with clear identification of single-phase and two-phase fields.

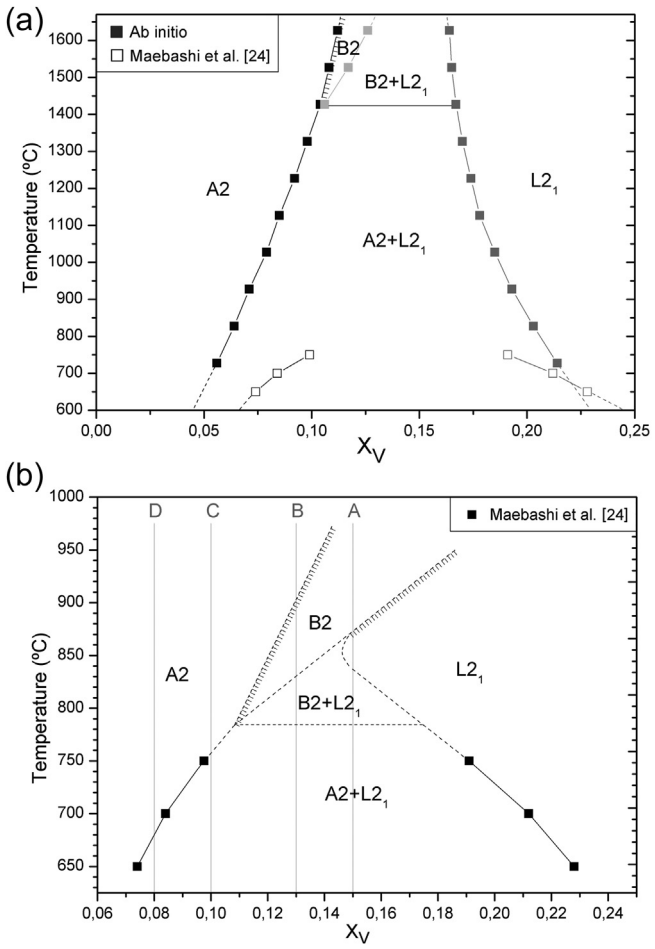

Fig. 2. Vertical $Fe_{1-2x}Al_xV_x$ section of the Fe–Al–V system. (a) Ab-initio calculations [33] and experimental data [24]. (b) Hypothetical vertical section built from the experimental data and the morphology of ab-initio calculations. Hatched lines represent second order transitions. Vertical gray lines indicate the nominal compositions of the studied alloys and named in Table 1.

Vickers micro hardness was determined after homogenization, solution and ageing treatments using a Leitz tester at loads between 0.98 y 1.96 N.

Phases identification in aged samples were investigated by transmission electron microscopy (TEM) using a PHILIPS CM200 operating at 160 or 200 kV and fitted with a double tilt holder. Thin foils for were prepared by cutting 3 mm diameter and 500 μm thickness discs using EDM, mechanically grinding the discs to 100 μm thickness, and final electrolytic thinning of the discs using a double-jet electro polisher STRUERS Tenupol-5 with an electrolyte comprising 67% methanol and 33% nitric acid. The polishing temperature was kept in the range −30 to −20 °C.

Since the $L2_1$ structure is a superlattice with regard to both the B2 and disordered A2 crystal structures, the $L2_1$ reciprocal lattice contains all the B2 and A2 reflections. Therefore, even when a mixture of phases was present, the superimposed diffraction patterns appear to be those only of the single $L2_1$ phase. In order, therefore, to distinguish between different phases and to generate contrast from different types of antiphase boundaries (i.e., $L2_1$ and B2 APBs), dark-field examinations were carried out using different diffraction **g** vectors of the [011] zone axis where the better contrast is obtained [36].

In order to calculate the average diameter and the volume fraction of $L2_1$ precipitates an accurate measurement of the foil thickness was needed. It was determined by using a convergent beam electron diffraction (CBED) technique looking for the intensity oscillations in the [hkl] disk and measuring the distance $\Delta\theta_i$ from the centre of the diffracted beam profile to each of the successive minima, together with the distance $2\theta_d$ between the centre

Table 1
Chemical compositions of the investigated $Fe_{1-2x}Al_xV_x$ alloys.

Alloy	Nominal composition (%at ± 0.001%at)			Measured composition Mean value (%at)			Standard deviation		
	Fe	Al	V	Fe	Al	V	Fe	Al	V
A	69.994	15.007	14.999	70.32	15.29	14.39	0.61	0.70	0.22
B	74.000	12.999	13.001	74.64	12.77	12.58	0.76	0.84	0.20
C	80.000	9.998	10.002	80.40	9.85	9.76	1.20	1.31	0.18
D	84.002	7.996	8.002	84.06	8.29	7.65	0.77	0.77	0.20

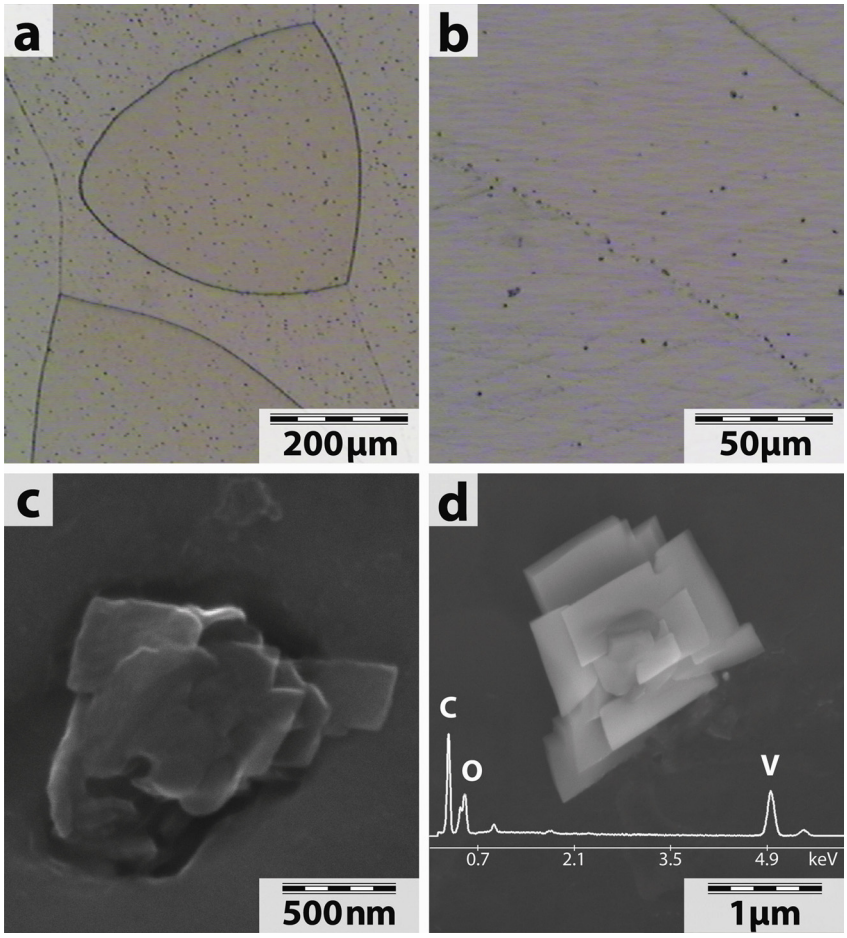

Fig. 3. Precipitation of vanadium carbides. (a) Optical micrograph of the alloy A after homogenization treatment at 1100 °C for 136 h. (b) Detail of the precipitation at the grain boundaries (alloy C). (d) SEM image of the carbide typical morphology. (e) Electron backscatter diffraction image of an extracted precipitate and its EDS spectrum.

spot [000] and the diffracted spot [hkl] [37]. From these measurements we obtained the deviation of the i-th minimum from the exact Bragg position $S_i = (\lambda/d_{hkl}^2)(\Delta\theta_i/2\theta_d)$ where λ is the wavelength and d_{hkl} is the spacing of the operating reflection. Finally, by using the two beam dynamic theory, the foil thickness t could be obtained from the intercept of the resulting straight line with the $(S_i/n_i)^2$ axis in a plot of $(S_i/n_i)^2$ versus $(1/n_i)^2$ where n_i is an integer. The average diameter of the precipitates was calculated assuming spherical particles and correcting for truncation effects induced by the limited foil thickness. This correction is accomplished by the following equation [38]

$$\overline{d} = \frac{2}{\pi}(d_{obs} - t) + \sqrt{\left(\frac{2}{\pi}(d_{obs} - t)\right)^2 + \frac{4d_{obs}t}{\pi}}$$

where $d_{obs} = (1/n_p)\sum_i^{n_p} d_i$ is the observed average diameter determined on a given area A of a micrograph and $\overline{d}$ is the corrected average diameter. The volume fraction, f_V, is then obtained through the spherical approximation [39]

$$f_V = \frac{4}{3}\pi\left(\frac{\overline{d}}{2}\right)^3 \frac{n_p}{At}$$

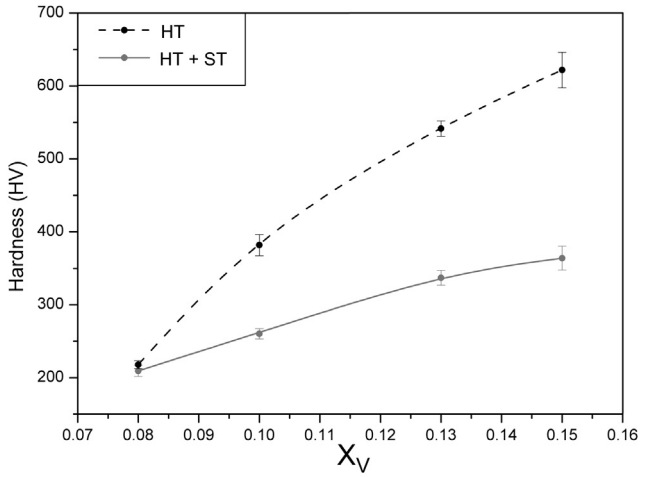

Fig. 4. Effect of V-content on micro-Vickers hardness of $Fe_{1-2x}Al_xV_x$ alloys with two heat treatment conditions. (Homogenization: heat treatment at 1100 °C for 136 h and cooling in air; Homo + Solution: the specimens in homogenization condition are afterwards heat treated at 1100 °C for 2 h and quenched in water).

4. Results and discussion

4.1. Microstructure and hardness after homogenization and solution treatment

The nominal and measured chemical composition of the alloys can be seen in Table 1. Both compositions appear equal within the experimental errors for the case of iron and aluminum while, for all

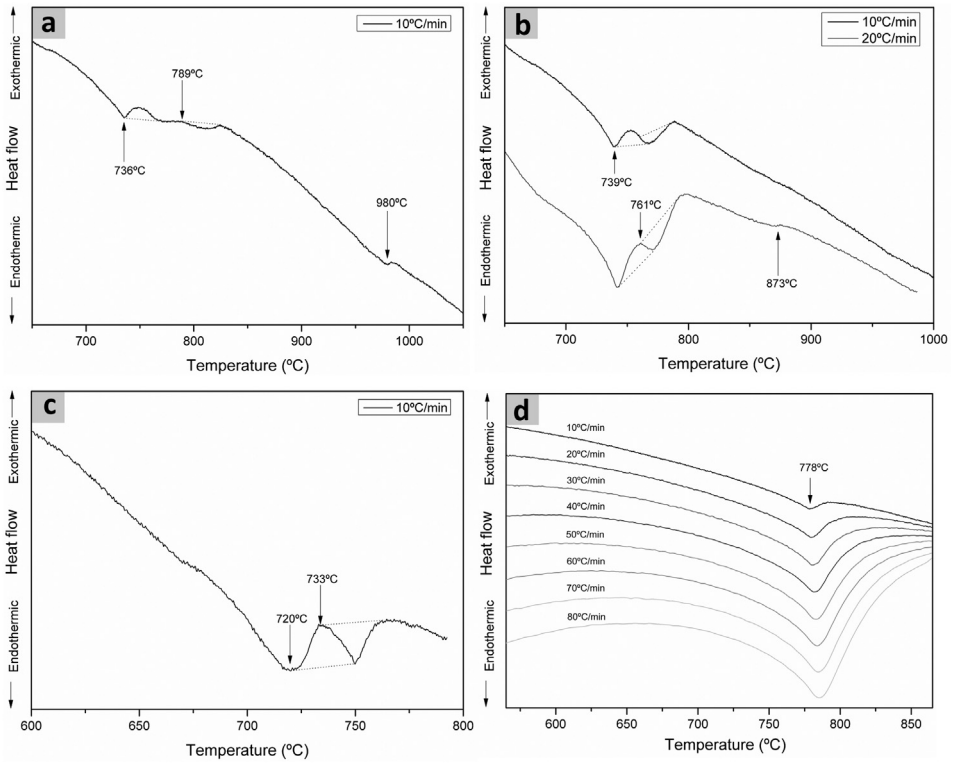

Fig. 5. DSC heating curves of $Fe_{1-2x}Al_xV_x$ alloys after solution treatment. (a) alloy A; (b) alloy B; (c) alloy C and (d) alloy D.

the alloys, the measured amount of vanadium is lower than the nominal. A widely varying dispersion of a second phase occurs in the matrix and also in the grain boundaries of all alloys regardless of the heat treatment (Fig. 3(a) and (b)). The range in size of the precipitates is between 1 and 0.5 μm (Fig. 3(c)) and the volume fraction is very low. These precipitates were extracted by the carbon replica method and isolated from the matrix for measuring their chemical composition by EDS (Fig. 3(d). The only metallic atom detected is Vanadium; the carbide composition cannot be quantified as the extraction replica also contains carbon. Our findings and information from the literature [40–42] allow us to infer that the precipitated phase is a vanadium carbide, carbon required for form it is perhaps provided as impurity (0.03 %at maximum) for the iron used to obtain the alloys.

The development of the hardness with composition and cooling rate from 1100 °C is shown in Fig. 4. The hardness increases with the aluminum and vanadium content regardless of the cooling rate, but the amount of vanadium carbides should decrease because the amount of iron in the alloys also decreases, so the hardness of the alloys cannot be related to the vanadium carbide dispersion. Instead of this and considering the hypothetical phase diagram section of Fig. 2(b), by increasing alloy content or by decreasing the cooling rate should be higher the precipitated fraction of the coherent phase Fe_2AlV and, as noted, greater hardness. This hypothesis will be validated with the findings that are reported in the following paragraphs.

Table 2
Results of the DSC investigations of the heat treated (1100 °C/2 h) alloys. Critical temperatures for phase transformation T_C and the anticipated phase transformations are indicated.

Alloy	T_{C1} (°C)	T_{C2} (°C)	T_{C3} (°C)
	$A2 + L2_1 \leftrightarrow B2 + L2_1$	$B2 + L2_1 \leftrightarrow B2$	$B2 \leftrightarrow A2$
A	736	789	980
B	739	761	873
C	720	733	–

4.2. Transformation temperatures

Fig. 5 shows the heating DSC curves for all the alloys. For the alloy A, three signals indicating phase transformations are observed. The first two signals, going from low to high temperatures and according with the area between the baseline and the DSC curve, may be associated with exothermic and endothermic transformations respectively. The third signal, at higher

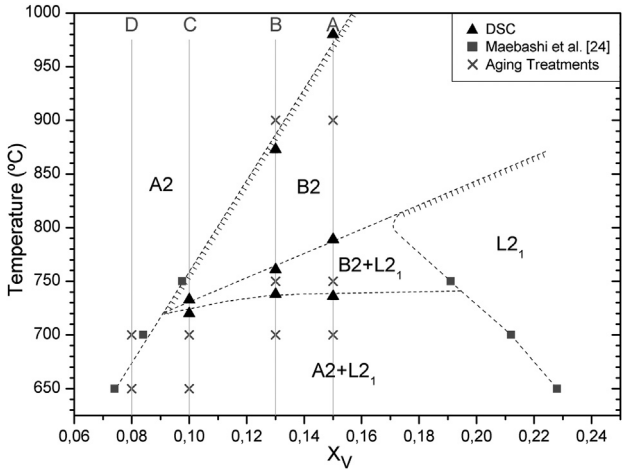

Fig. 6. Assessment of the vertical $Fe_{1-2x}Al_xV_x$ section based on ab-initio calculations [33], experimental data [24] and DSC measurements. The cross symbol indicates each aging treatment proposed for TEM examination.

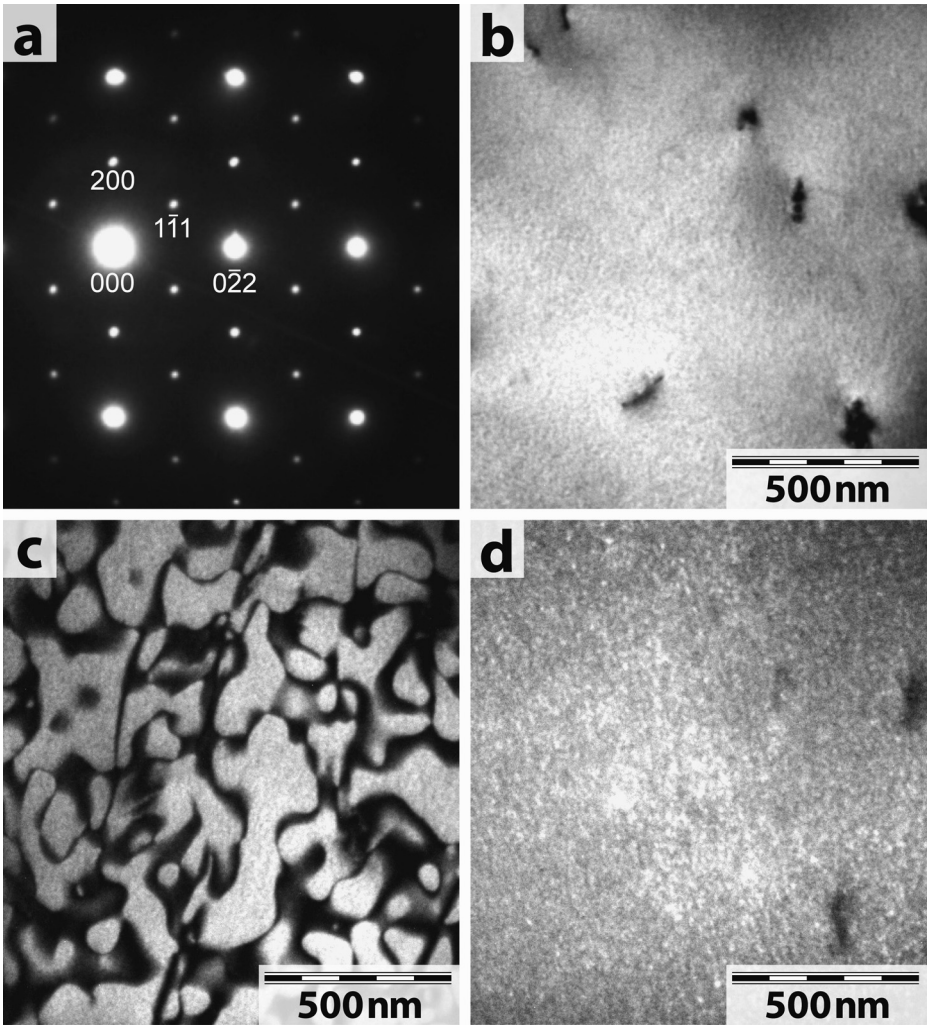

Fig. 7. TEM micrographs of A alloy as-quenched from 1100 °C after 2 h. B2 APBs formed when the B2 phase field is crossed during cooling. (a) (0 1 1) **DP**; (b) **BF**; (c) [2 0 0] **DF**; (d) [1 1 1] **DF**.

temperature, has the characteristic shape of a second order order-disorder transition [43]. Similar signals are observed in the B alloy when the heating rate is increased to 20 °C/min. Instead of this, alloy C has lost the signal of the second order order-disorder transition. Finally, alloy D has lost the three signals but displays a new signal at 778 °C which can be attributed to the dissolution of vanadium carbides [39]. This signal is only detected in the alloy D because the iron content is greater than in other alloys and then, as was discussed in the preceding paragraph, the amount of carbon available to form carbides is greater.

The determined critical temperatures for phase transformations T_C are summarized in Table 2. The association between a critical temperature and a specific phase transition is done based on the hypothetical phase diagram section of Fig. 2(b) and it must be validated with TEM examination at room temperature of the quenched microstructure of aged samples.

Some edges of the phase fields in the hypothetical phase diagram section can now be adjusted with the results of Table 2. This modification is shown in Fig. 6 along with the aging treatments proposed for TEM examinations. These aging treatments were planned to be located in all the fields present in the phase diagram section. The solution treatment at 1100 °C/2 h, which were previously performed at the four alloys, may also be regarded as an aging treatment.

4.3. Phases identification after solution and ageing treatment

In what follows we discussed TEM observations studying the transformations as the temperature decreases.

The A alloy as-quenched from 1100 °C after 2 h of heat treatment reveal the presence of the superlattice reflection spots of the ordered $L2_1$ phase as is shown by the diffraction pattern (DP) of Fig. 7(a), this means that the A2 disordered structure present at high temperatures could not be retaining by quenching. The order-disorder transformations of the system have a very high transformation speed and the ordering reactions start during cooling [44]. In the bright field (BF) image (Fig. 7(b)), needle shaped vanadium carbide precipitates are observed oriented along three mutually orthogonal directions, these carbides appear in the TEM micrographs of all alloys investigated and not be included in the phase's analysis. The [200] dark-field (DF) image (Fig. 7(c)) shows B2 antiphase domain boundaries (APBs) formed when the B2 phase field is crossed during cooling. The [111] DF (Fig. 7(d)) exhibits bright speckles about 2–10 nm in size which are the image features of short-range order in a disordered matrix [45]. The same conditioning treatment on alloy B gives, in TEM observations, similar characteristics to those of alloy A but with specific changes: the $L2_1$ superlattice reflections appear more diffuse and less intense (Fig. 8(a)) and the B2 antiphase domains are smaller (Fig. 8(b)).

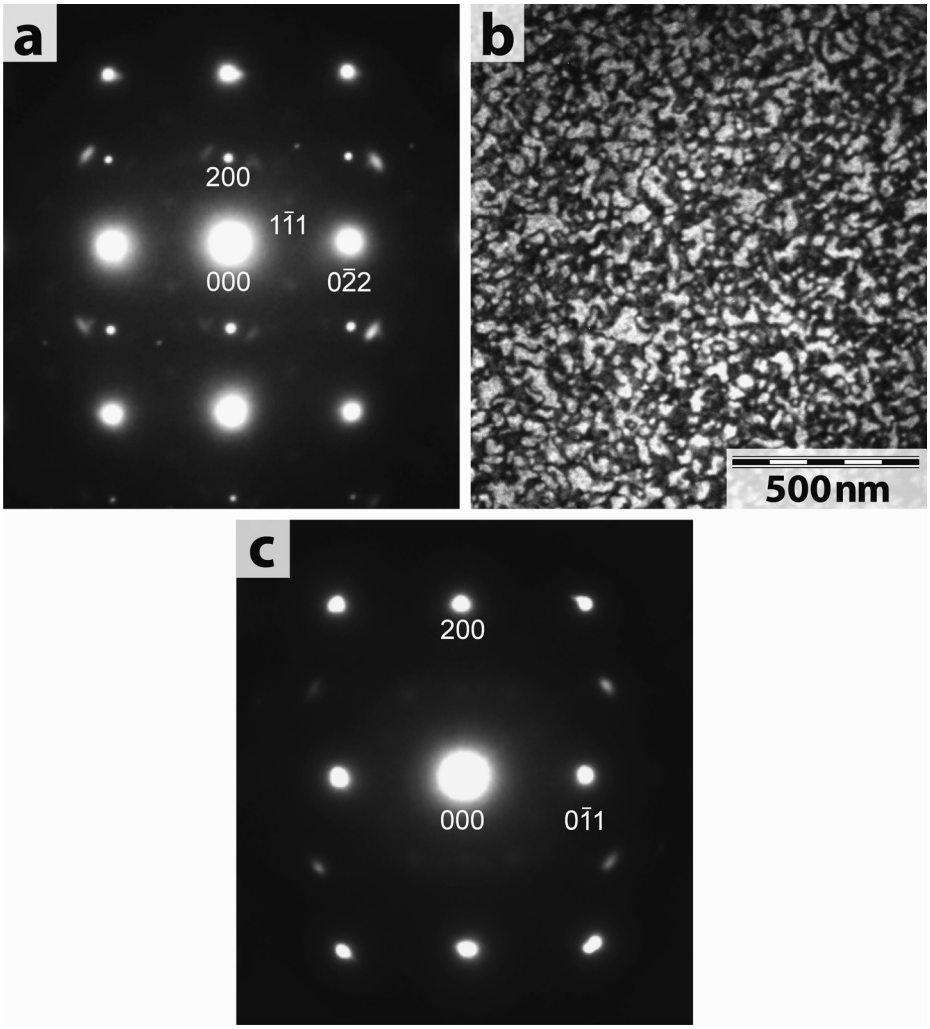

Fig. 8. TEM micrographs of alloys B, C and D as-quenched from 1100 °C after 2 h (a) (0 1 1) **DP** of alloy B, $L2_1$ superlattice reflections appear diffuse and weak. (b) [2 0 0] **DF** of alloy B, B2 APBs are smaller than in alloy A. (c) (0 1 1) **DP** of alloys C or D show neither $L2_1$ nor B2 ordered phase spots.

Finally, the alloys C and D quenched from 1100 °C show neither $L2_1$ nor B2 ordered phase spots in the DP (Fig. 8(c)). All of these findings are in excellent agreement with the hypothetical phase diagram section of Fig. 6; all the alloys are in the A2 field at 1100 °C; A, B and C alloys cross the B2 phase field and observations of decreasing B2 antiphase domains until their disappearance agrees with decreasing width of the B2 phase field when the addiction of Al (V) decreases; evidence of $L2_1$ short-range order rather than $L2_1$ APBs suggest that B2 → $L2_1$ order-disorder transformation occurs at $X > 0.15$; lastly the $L2_1$ short-range order is fostered by the prior order-disorder transition A2 → B2. However, the failure to observe neither B2 APBs nor B2 order spots in the diffraction pattern of alloy C deserves a warning, as there may be another explanation than the obvious narrow width of the B2 phase field.

Both alloys A and B quenched from 1100 °C and aged at 900 °C/1 h shows $L2_1$ ordered phase spots in their DPs and their [111] DFs images exhibit bright speckles (Fig. 9(a) and (b)). However, their [200] DFs differ (Fig. 9(c) and (d)), in alloy A the B2 APBs have disappeared because the ordering reactions take place at the annealing temperature and there is time for the antiphase domains to grow much larger, usually larger than a selected area of TEM observation. Then, at 900 °C the alloy A is on the B2 field and the alloy B is on the A2 field in agreement with our hypothesis about the $Fe_{1-2x}Al_xV_x$ section.

A two-phase microstructure is observed in both alloys A and B quenched from 1100 °C and aged at 750 °C/1 h (Fig. 10), in the case of alloy B the [111] DF shows bright spherical precipitates within the matrix while in the alloy A the bright precipitates looks wormy. In the [200] DF image the matrix become gray and APBs are visible indicating that it should have the B2 phase structure. So, both alloys A and B are in the two-phase region (B2 + $L2_1$) at 750 °C as was proposed in Fig. 6.

Once again a two-phase microstructure is observed in both alloys A and B quenched from 1100 °C and aged at 700 °C/2 h (Fig. 11). Now, the $L2_1$ ordered phase spots in their DPs are more concentrated and intense; their [111] DFs images exhibit bright precipitates which morphologies are similar to that observed in these alloys aged at 750 °C but in the [200] DFs images the matrix become dark indicating that it has the A2 phase structure. The alloy C quenched from 1100 °C and aged at 700 °C/2 h does not show the $L2_1$ ordered phase spots in it DP that means the A2 solvus line in the hypothetical phase diagram section must be close to the point $X \approx 0.10$ and $T \approx 700$ °C. The last assumption is confirmed with the results of the observations in alloys C and D quenched from 1100 °C and aged at 650 °C/2 h. In alloy C both DFs images show bright spherical precipitates within a black matrix (Fig. 12(a) and (b)). Accordingly, the microstructure consists of A2 matrix and $L2_1$ precipitates. Instead of this, the DP of alloy D does not exhibit any

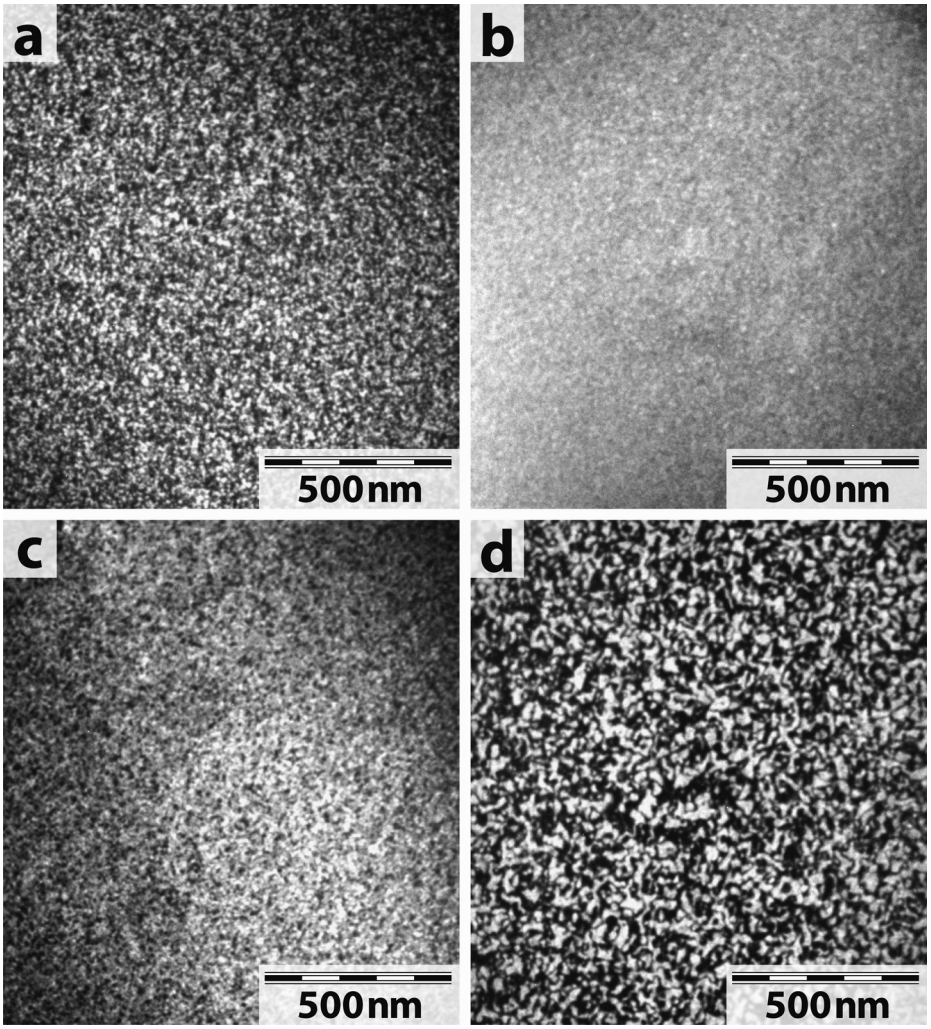

Fig. 9. TEM micrographs of alloys A and B aged at 900 °C/1 h. (a) and (b) [1 1 1] **DF** of alloys A and B respectively, only a bright speckle is observed. (c) [2 0 0] **DF** of alloy A, B2 APBs have disappeared. (d) [2 0 0] **DF** of alloy B, B2 APBs is still present.

kind of superlattice reflection (Fig. 12(c)) pointing out that the alloy D is on the A2 field at 650 °C.

The transition sequences and temperatures determined in all the present alloys indicate the need for a reassessment of the $Fe_{1-2x}Al_xV_x$ section for $X \leq 0.10$. First, the A2 solvus line is moved to higher value of X in order to become closer the alloy C at 700 °C and leave alloy D in the A2 field at 650 °C. This modification causes that, to the composition of alloy C, the single phase field B2 disappears and then the phase transitions of alloy C at 733 °C and 720 °C have to be defined again. Our assumption is that the (A2 + B2) two-phase field which exist in the binary Fe–Al alloy also may exist within very narrow temperature and composition limits in the ternary Fe–Al–V system. So, the new assessment of the $Fe_{1-2x}Al_xV_x$ section is shown in Fig. 13 together with a scheme of the Fe–Al–V isothermal section at 735 °C depicting the influence of that modification. The position of the B2 solvus line is only speculative and not proven in this work, in what follows we discuss results that are affected by this choice. Note that during heating of alloy C the first transition is (A2 + $L2_1$)→(A2 + B2) and occurs at 720 °C, here a low mass fraction of $L2_1$ precipitates become less ordered but a higher mass fraction of B2 precipitation appears (the B2 solvus is closer to the nominal composition of alloy C than the $L2_1$ solvus), this means that a order transformation is predominant giving a exothermic DSC signal as shown in Fig. 5(c). With increasing temperature, the alloy C reaches the second transition (A2 + B2) → A2 at 730 °C, the B2 precipitates become disordered, leaving only A2 phase, as seen in the endothermic DSC signal of Fig. 5(c). In turn, the absence of the B2 APBs and $L2_1$ order spots in the TEM observations of C alloy quenched from 1100 °C is justified with these modifications of the phase diagram because now the cooling path of the alloy C does not cross the B2 single phase field. Finally, and even with these changes, there is a disagreement between the experimental results and the assessment of the $Fe_{1-2x}Al_xV_x$ vertical section in Fig. 13. The alloy C aged at 700 °C shows no precipitation of $L2_1$ phase, in our opinion, due to the proximity of the A2 solvus to the aging conditions since minor fluctuations in composition and temperature during the heat treatment can prevent precipitation of $L2_1$ phase.

4.4. Hardness after ageing treatments

The variation of micro-Vickers hardness (HV) with heat treatment condition and (Al + V) content was also investigated to foresee the effect of the $L2_1$ phase precipitation on mechanical properties of $Fe_{1-2x}Al_xV_x$ alloys. The measured hardness values were summarized in Fig. 14.

The alloys in the condition as-quenched from 1100 °C after 2 h of heat treatment show the lower hardness values which increase with the content of (Al + V). Alloys C and D have A2 phase and do

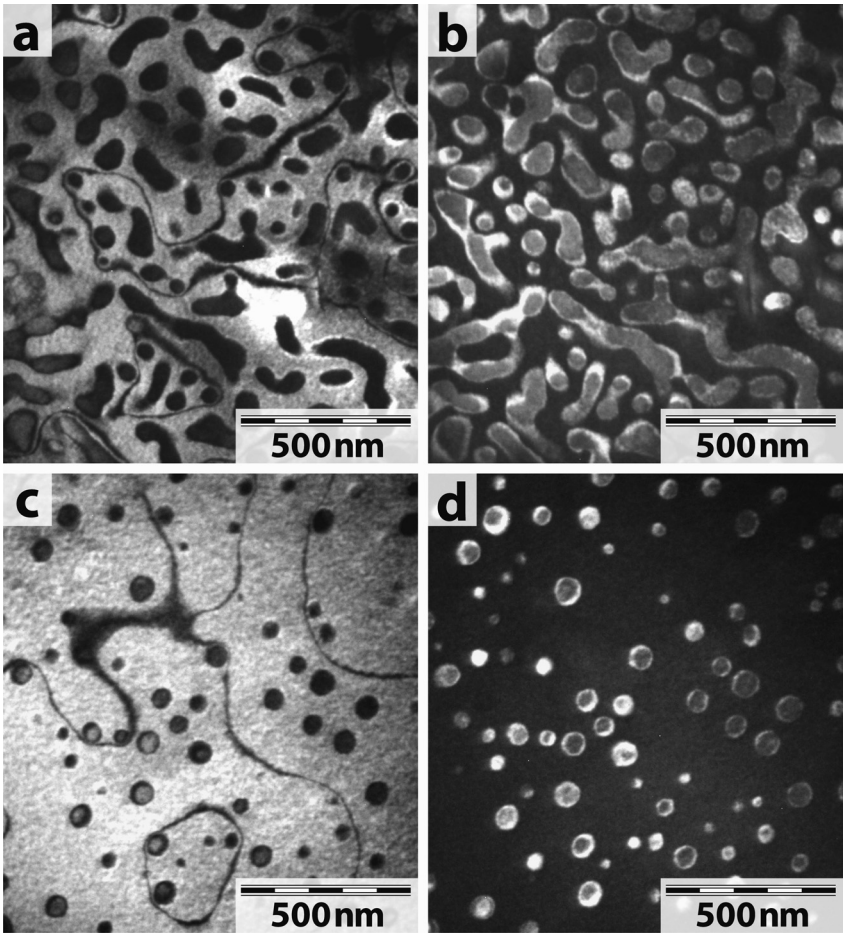

Fig. 10. TEM micrographs of alloys A and B aged at 750 °C/1 h. Alloy A, (a) [2 0 0] **DF** and (b) [1 1 1] **DF**, wormy-shaped $L2_1$ phases are formed in the B2 matrix. Alloy B, (c) [2 0 0] **DF** and (d) [1 1 1] **DF**, spherical-shaped $L2_1$ phases are formed in the B2 matrix.

not undergone phase transformations during cooling then, the hardness increment may be only consequence of solid-solution hardening at concentrated solutions ($c^{2/3}$ dependence, i.e Labusch's model [46]). The same hardening mechanism on alloys A and B having a B2 ordered phase would give a drop in the hardness values because the strength at room temperature decreases with increasing degree of long-range order [47], but this is not observed. Therefore we believe that two extra strengthening mechanisms must be added: B2 APB domain hardening [48] which, by comparing the domain size, should be higher for the B alloy and the destruction by slip dislocations of any existing $L2_1$ short-range order $((c^*(1-c))^2$ dependence, i.e Flinn's model [49]).

The hardness values for the alloys quenched from 1100 °C and aged at 700 °C/2 h increases as the volume fraction of $L2_1$ phase precipitates does. At low (Al + V) content there is not precipitation and the hardness values are close to those of as-quenched condition. Then, there is a strong increment of hardness for alloy B (point #1) as consequence of $L2_1$ spherical precipitation on A2 matrix (Fig. 11(c)) but the rate of hardening decreases with further $L2_1$ volume fraction (point #2) because the A alloy exhibit over-aging, that is, there is coalescence of precipitates resulting in an elongated and branched morphology (Fig. 11(a)). The last behavior is pointing out that the precipitation kinetics is dependent of the volume fraction [50] and then the ageing time for the maximum attainable hardness must be determinate for each case. To emphasize this point, we show that the alloy C aged for 2 h at 650 °C achieved similar hardness values (point #3) even with lower volume fraction of $L2_1$ phase. We also note that all hardenable $Fe_{1-2x}Al_xV_x$ alloys show, at room temperature, hardness values comparable to those obtained in the alloy Fe–23Al–8.5Ti.

Finally, the low hardness produced by precipitation of $L2_1$ phase in the B2 matrix as measured on the alloys A and B after quenched from 1100 °C and aged at 750 °C/1 h (points #4 and #5) is proof that, at room temperature, the A2 phase is harder than the fully ordered B2 matrix.

4.5. Evaluation of the strengthening mechanism at room temperature

In the preceding paragraph the hardening of alloys has been qualitatively interpreted as a result of the volume fraction and morphology of the $L2_1$ precipitation. To quantitatively evaluate this hypothesis, the average size and the volume fraction of the spherical precipitates of alloys B and C were calculated by using the measurements outlined in the Section 3. Table 3 shows these results together with the equivalent maximum pressure σ^H obtained from the Vickers micro-hardness measurements of Fig. 14. Clearly the hardness increases as do the size and volume fraction of $L2_1$ precipitates.

It was reported in early studies of NiAl-B2 strengthened Fe–20Cr–2Ni–1Al [51] and Fe–23Al–6Ni [52] ferritic steels that the precipitates are sheared by dislocations up to peak strength and then, for overaged conditions, the particles were bypassed by dislocation loops. Because both B2 and $L2_1$ phases precipitate in the

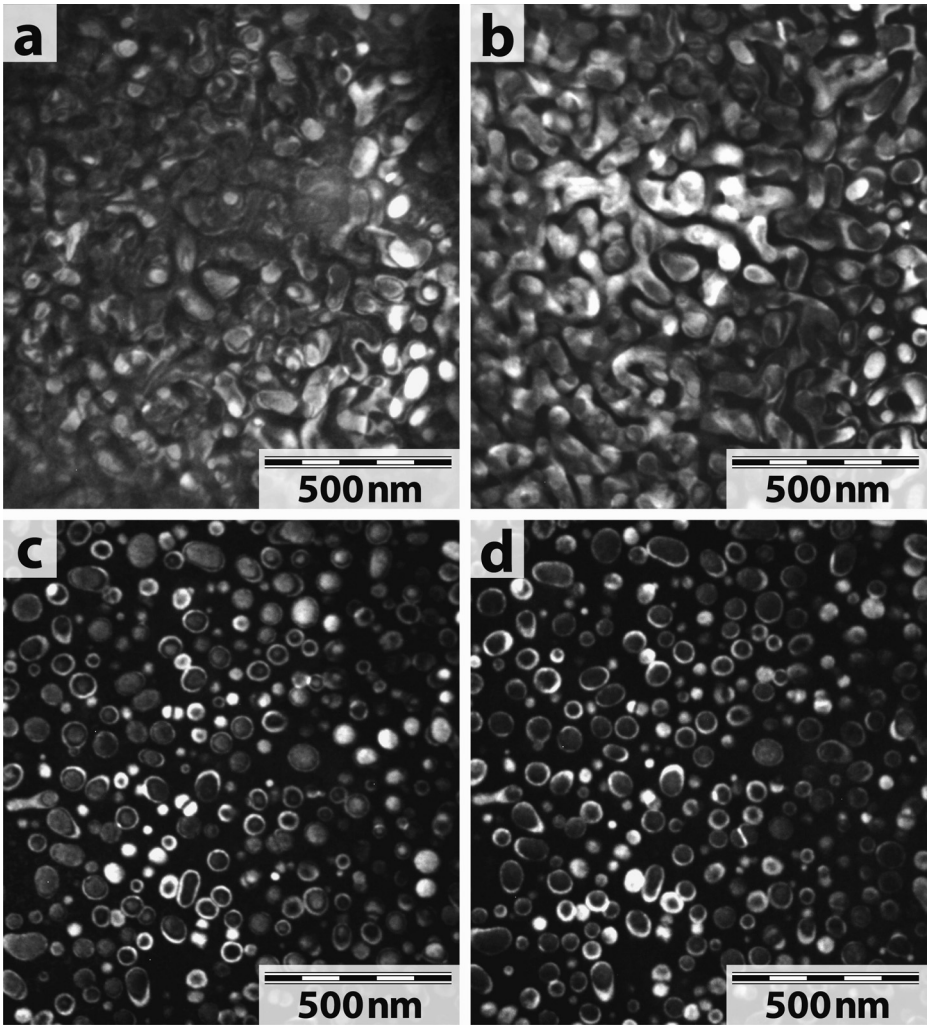

Fig. 11. TEM micrographs of alloys A and B aged at 700 °C/2 h. Alloy A, (a) [2 0 0] **DF** and (b) [1 1 1] **DF**, wormy-shaped $L2_1$ phases are formed in the A2 matrix. Alloy B, (c) [2 0 0] **DF** and (d) [1 1 1] **DF**, spherical-shaped $L2_1$ phases are formed in the A2 matrix.

matrix of α-(Fe, Al) satisfying the same relation cube-on-cube with small misfit strain, we expect the same hardening mechanism for the $Fe_{1-2x}Al_xV_x$ alloys of this work even though we have no experimental evidence.

In general, precipitation hardening in metals where dislocations shear precipitates depends on the details of the interactions between the dislocations and the particles. The major contributions to that interaction could come from coherency strains [53,54], modulus mismatch [55] and APB energy in sheared particles [50,51]. These strengthening contributions will now be considered in the light of existing theories and compared against our results. Before, it is necessary to assess the magnitude of precipitation hardening as it appears in theoretical models, this is, the increase in critical resolved shear stress (CRSS) $\Delta\tau_p$. For every age-hardened condition the yield strength of the material is related to the $\Delta\tau_p$ through the relationship $\sigma_{ys} = \sigma_0 + M\,\Delta\tau_p$ where σ_0 is the yield strength of the solution annealed material (i.e. without hardening precipitates and with solute impoverishment) and M is the Taylor factor, which for bcc materials is approximately 2.9. Finally, we propose to estimate the yield stress from the hardness through Tabor's empirical relationship $\sigma^H \sim 3\,\sigma_{ys}$. Therefore, it is possible to estimate $\Delta\tau_p$ for every aged condition with the equation $\Delta\tau_p \approx (1/3M)(\sigma^H_{ys} - \sigma^H_0)$. In our analysis, σ^H_0 was estimated from the hardness values of alloy D in Fig. 14 for the same ageing treatment of alloys B and C (see Table 3). This assumption was taken because alloy D has a composition close to the A2 solvus and has not shown any precipitates for these ageing treatments.

Several other assumptions, taking data from literature, ought to be made in order to compare the experimental results with theoretical calculations. The lattice parameter, a_m, and Young modulus of the matrix, E_m, were taken from data for the α-(Fe, Al) disordered solid solution at $x_{Al} = 0.16$ considering that the composition of the matrix is that of alloy D and V atoms behave like Al atoms, then $a_m = 0.2885$ nm [56], $E_m = 163$ GPa [57]. For the precipitate we took $a_p = 0.5761$ nm which is the lattice parameter of the $L2_1$ phase [58] and $E_p = 328$ GPa which is a theoretical value for the Fe_2AlV intermetallics obtained by first principles calculation [59]. For both phases the Poisson modulus ν was set at 1/3 and the shear modulus was evaluated as $G = E/2(1+\nu)$.

In order to estimate the coherency strengthening contribution, we applied the model proposed by Brown and Ham [50] for the shear stress to cut a coherent precipitate:

$$\Delta\tau_{\text{coherency}} = \alpha G_m |\varepsilon|^{3/2} \left(\frac{f_V \bar{d}}{2b}\right)^{1/2} \quad (1)$$

where $\alpha = 4.1$, G_m is the shear modulus of the matrix and $b = (a_m/2)\langle 111\rangle = 0.2498$ nm is the length of the Burgers vector of the bcc matrix. In addition, ε is the misfit parameter, which is given by

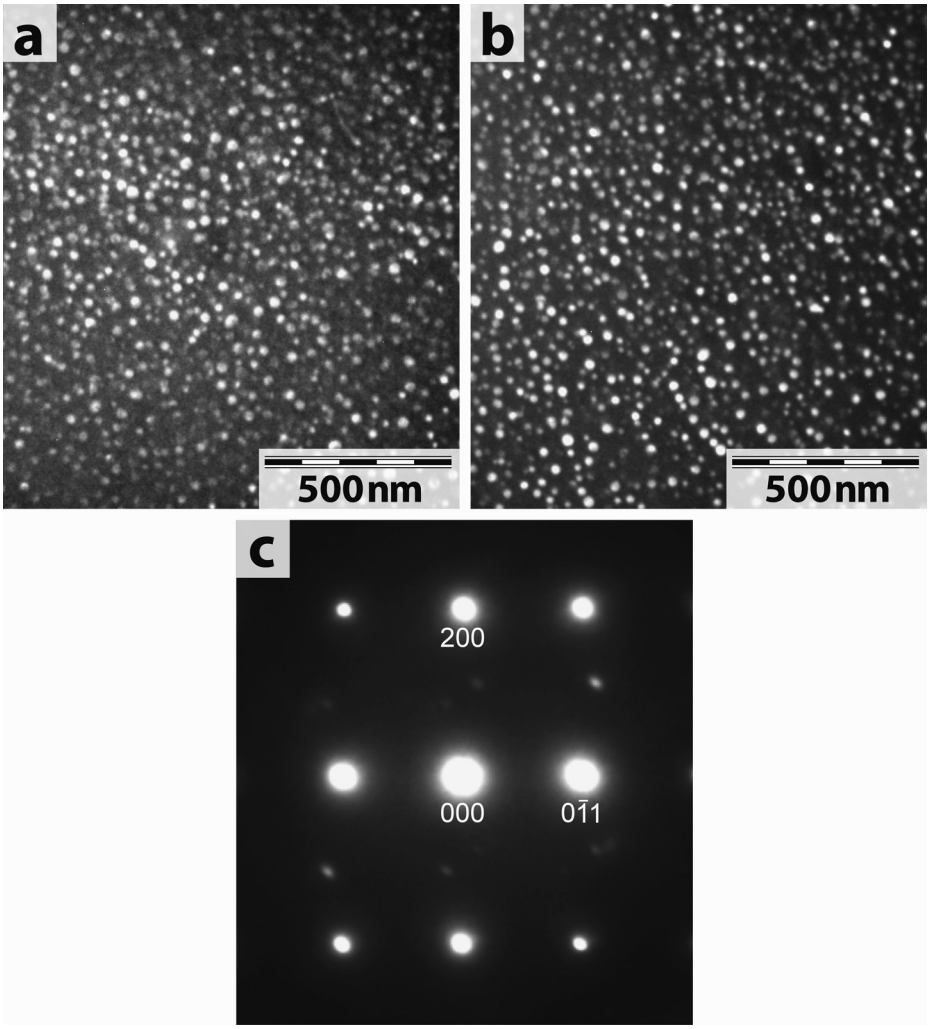

Fig. 12. TEM micrographs of alloys C and D aged at 650 °C/2 h. Alloy C, (a) [2 0 0] **DF** and (b) [1 1 1] **DF**, spherical-shaped $L2_1$ phases are formed in the A2 matrix. (c) (0 1 1) **DP** of alloy D show neither $L2_1$ nor B2 ordered phase spots.

$$\varepsilon = \frac{2}{3}\frac{(a_p/2) - a_m}{a_m} \tag{2}$$

Substituting the constant values into Equations (1) and (2) leads to a shear stress increment of 0.020 GPa for the alloy B which is small compared with the strengthening determined experimentally.

The large shear modulus mismatch between matrix and precipitate $\Delta G/G_m \approx 1$ suggests that shear modulus hardening could operate. For this contribution, we applied the model used by Nembach [55]:

$$\Delta\tau_{\text{modulus}} = \beta(\Delta G)^{3/2}\left(\frac{f_V}{T}\right)^{1/2} b\left(\frac{\bar{d}}{2b}\right)^{3n/2-1} \tag{3}$$

where $\beta = 0.0055$ and $n = 0.81$ are constant and $T = G_m b^2/2$ is the line tension of dislocation. This approach gives an increment in shear stress of 0.353 GPa for the alloy B which can correspond to the observed precipitation strengthening. However, this result must be taken with care because the Young modulus of the precipitate is calculated for 0 K while the measured data point is for room temperature (298 K) and because the splitting of dislocations into partials inside the precipitate will reduce the effect of the modulus difference still further [57].

If a $1/2\langle 111\rangle$ dislocation cuts the Fe_2AlV precipitates, an APB is left inside the precipitates. An additional stress is required to drag the APB, which can be estimated by the following expression [51]

$$\Delta\tau_{\text{order 1}} = \left(\frac{\gamma_{APB}}{b}\right) - \frac{2T}{b\sqrt{2/3}\bar{d}} \tag{4}$$

where γ_{APB} is the APB energy per unit area on the [110] plane. However, if paired $(1/2)\langle 111\rangle$ dislocations passed through the precipitates no APB is left inside the precipitates and the shear stress increment is given by Ref. [50],

$$\Delta\tau_{\text{order 2}} = \frac{\gamma_{APB}}{2b}\left[\left(\frac{2\gamma_{APB}\bar{d}f_V}{\pi T}\right)^{1/2} - f_V\right] \tag{5}$$

Note that γ_{APB} is experimentally unknown for Fe_2AlV but we have access to theoretical values for Fe_2AlNb and Fe_2AlTi recently obtained by first principles calculation [60]. These values are 0.64 J/m^2 and 0.57 J/m^2 respectively. Since γ_{APB} is directly proportional to the ordering energy and the three intermetallics have the same crystal structure we can infer a value for Fe_2AlV through comparison of their ordering energy calculated with the same theoretical method [33], these values are −48.69 kJ/mol (Fe_2AlTi); −43.40 kJ/

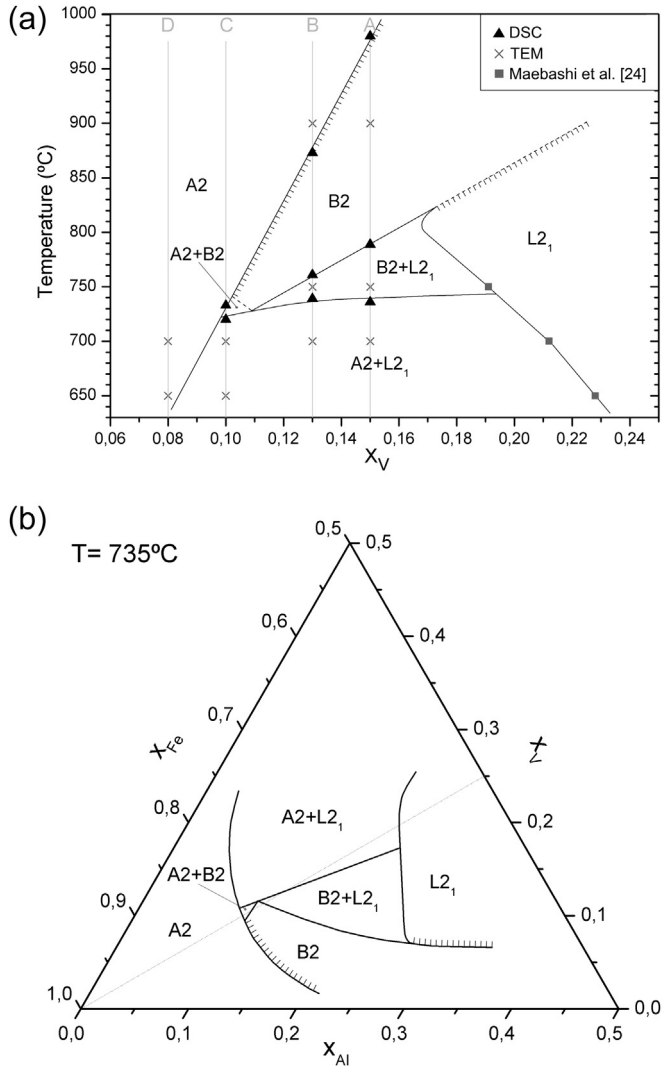

Fig. 13. (a) Assessment of the vertical $Fe_{1-2x}Al_xV_x$ section based on ab-initio calculations [33], experimental data [24], DSC measurements and TEM observations of aged specimens. (b) Scheme of the Fe–Al–V isothermal section at 735 °C including the estimated (A2 + B2) region.

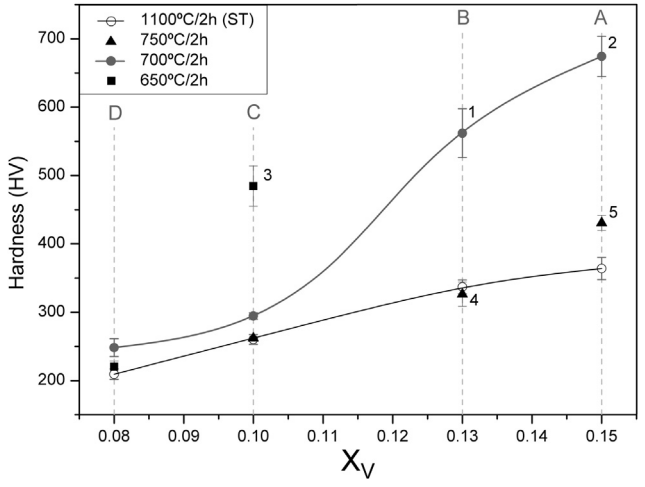

Fig. 14. Effect of V-content and ageing temperature on micro-Vickers hardness of solution treated $Fe_{1-2x}Al_xV_x$ alloys.

Table 3
Values of the precipitate volume fraction f_v, average particle diameter $\overline{d}$ and CRSS increment $\Delta\tau_p$.

Alloy	Ageing treatment	$\overline{d}$ nm	f_v	Vickers hardness, HV	σ^H GPa	$\Delta\tau_p$ GPa
B	2 h at 700 °C	58 ± 3	0.29 ± 0.07	562 ± 36	5.5 ± 0.4	0.36 ± 0.06
D	2 h at 700 °C	–	–	248 ± 13	2.4 ± 0.1	–
C	2 h at 650 °C	24 ± 3	0.10 ± 0.02	485 ± 30	4.8 ± 0.3	0.29 ± 0.04
D	2 h at 650 °C	–	–	221 ± 8	2.26 ± 0.08	–

mol (Fe_2AlV) and −40.10 kJ/mol (Fe_2AlNb). This comparison indicates that the value of the APB energy for Fe_2AlV would be the average of the values for the other two intermetallics, this is $\gamma_{APB} = 0.61$ J/m^2. Using this value of γ_{APB} in Equations (4) and (5) with the morphological parameters of alloy B gives very high values for the order strengthening contribution, thus one can concluded that both alloys C and B are in overaged condition and therefore the Orowan mechanism could explain their hardness.

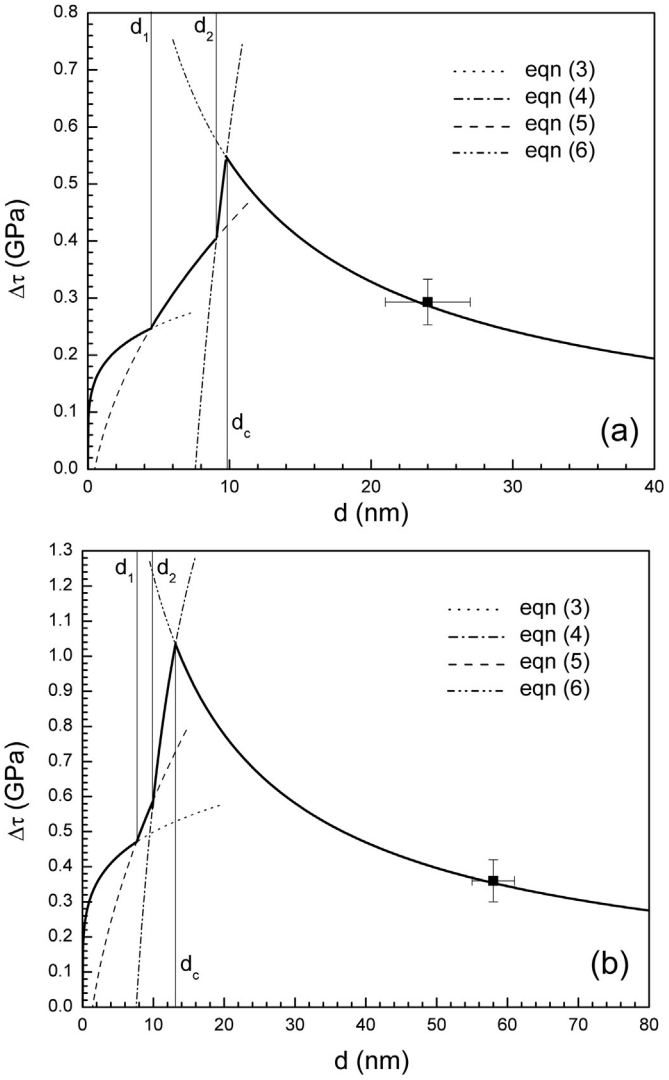

Fig. 15. Theoretically estimated CRSS as a function of particle diameter in $Fe_{1-2x}Al_xV_x$ alloys containing spherical coherent Fe_2AlV-$L2_1$ ordered particles in precipitated volume fractions of (a) $f_V = 0.10$ and (b) $f_V = 0.29$. Data points from Table 3. Thin lines: models of proposed active mechanism of strengthening. See text. Thick line: proposal for the overall evolution of the hardening with the particle diameter.

Among several estimates for the Orowan stress [61], we have chosen the model proposed by Ashby [62] which accounts for the statistical distribution of the particles in the glide plane and the mutual loop interaction:

$$\Delta\tau_{\text{Orowan}} = 0.84\frac{G_m b}{L}\frac{(2-\nu)}{4\pi(1-\nu)}\ln\left(\frac{\overline{\overline{d}}}{b}\right) \quad (6)$$

with $L = \overline{d}(0.724 f_V^{1/2} - 0.816)$ and $\overline{\overline{d}} = (\overline{d}^{-1} + L^{-1})^{-1}$. Fig. 15 shows the theoretically estimated increase of CRSS in alloys C and B according to Equations (3)–(6), in both cases the result suggests that there are three controlling interaction mechanisms as function of the diameter for underaged particles. First there is a transition at d_1 from the shear modulus hardening to order strengthening by coupled dislocation pairs, and then a second transition appears at d_2 where the dominant mechanism is the 'cut-in' stress required for the leading dislocation of the strongly coupled pair to penetrate the ordered particle. Finally, beyond a critical diameter d_c the Orowan process is favored since the Orowan stress becomes smaller than the 'cut-in' stress. As it can observed, the hardness value of both alloys B and C lie on the Orowan curve showing that they own overaged particles. Furthermore, this evaluation shows that the maximum hardness for each volume fraction is found for smaller sizes of precipitates that can be achieved by reducing the heat treatment time.

5. Conclusions

The present study was primarily focused on an evaluation of the microstructures at different temperatures and compositions of $Fe_{1-2x}Al_xV_x$ alloys in view of strengthening by coherent particle. The obtained results lead to the following conclusions:

a) Phase separation into disordered A2 and ordered $L2_1$ phases occurs for $0.10 < X < 0.15$ for temperatures lower than 720 °C. Above this temperature and with increasing X in the same range of composition may appear the following regions: (A2 + B2), B2 and (B2 + $L2_1$).
b) The alloys quenched from 1100 °C and aged at 700 °C/2 h show spherical precipitates of $L2_1$ phase for $X < 0.125$, for larger values of X over-aging is observed.
c) The hardness values, measured at room temperature, for the alloys with $X < 0.125$ and ageing temperature between 650 and 700 °C are comparable to those obtained in the alloy Fe–23Al–8.5Ti.
d) The alloys quenched from 1100 °C and aged in the (B2 + $L2_1$) region show, at room temperature, a very low increment of hardness.
e) The strengthening mechanism at room temperature was evaluated under the assumption that the precipitates are sheared by dislocations up to peak strength and then, for overaged conditions, the particles were bypassed by dislocation loops. The evaluation consisted of the prediction in the light of existing theories and the comparison against our results. The result of this evaluation points out that the alloys with $X < 0.125$ and heat treatment of 2 h between 700 and 650 °C have overaged and the calculated Orowan stress accounts for the variation in the increment of SCRR with particle size and volume fraction. Furthermore, the evaluation shows that the maximum hardness for these alloys may be found at smaller size of the precipitates by reducing the heat treatment time in the same temperature range. Future work should be done to confirm this latter conclusion.

These findings leave open a window on composition and temperature where the mechanical properties of the Fe–Al based alloys can be improved by the addition of vanadium.

Acknowledgments

PAF was supported by a UNSAM/CNEA master fellowship. We greatly appreciate Dr. C.G. Schön for giving access to his computer code cvm17bf2a (ternary equilibrium).

References

[1] Sauthoff G. Intermetallics. Weinheim: Wiley-VCH; 1995. p. 1.
[2] Deevi SC, Sikka VK. Nickel and iron aluminides: an overview on properties, processing, and applications. Intermetallics 1996;4:357–75.
[3] Stoloff NS. Iron aluminides: present status and future prospects. Mater Sci Eng A 1998;258:1–14.
[4] Morris DG. Possibilities for high-temperature strengthening in iron aluminides. Intermetallics 1998;6:753–8.
[5] Palm M. Concepts derived from phase diagram studies for the strengthening of Fe-Al-based alloys. Intermetallics 2005;13:1286–95.
[6] Morris DG, Muñoz-Morris MA. Recent developments toward the application of iron aluminides in fossil fuel technologies. Adv Eng Mater 2011;13:43–7.
[7] Lawley A, Coll JA, Cahn RW. Influence of crystallographic order on creep of iron aluminum solid solutions. Trans AIME 1960;218:166–76.
[8] Eumann M, Palm M, Sauthoff G. Alloys based on Fe_3Al or FeAl with strengthening Mo_3Al precipitates. Intermetallics 2004;12:625–33.
[9] Risanti DD, Sauthoff G. Strengthening of iron aluminide alloys by atomic ordering and Laves phase precipitation for high-temperature applications. Intermetallics 2005;13:1313–21.
[10] Stein F, Palm M, Sauthoff G. Mechanical properties and oxidation behaviour of two-phase iron aluminium alloys with $Zr(Fe,Al)_2$ Laves phase or $Zr(Fe,Al)_{12}$ τ_1 phase. Intermetallics 2005;13:1275–85.
[11] Schneider A, Falat L, Sauthoff G, Frommeyer G. Microstructures and mechanical properties of Fe_3Al-based Fe–Al–C alloys. Intermetallics 2005;13:1322–31.
[12] Krein R, Schneider A, Sauthoff G, Frommeyer G. Microstructure and mechanical properties of Fe_3Al-based alloys with strengthening boride precipitates. Intermetallics 2007;15:1172–82.
[13] Risanti DD, Sauthoff G. Microstructures and mechanical properties of Fe–Al–Ta alloys with strengthening Laves phase. Intermetallics 2011;19:1727–36.
[14] Morris DG, Requejo LM, Muñoz-Morris MA. A study of precipitation in $D0_3$ ordered Fe–Al–Nb alloy. Intermetallics 2005;13:862–71.
[15] Morris DG, Muñoz-Morris MA. Room and high temperature deformation behaviour of a forged Fe–15Al–5Nb alloy with a reinforcing dispersion of equiaxed Laves phase particles. Mater Sci Eng A 2012;552:134–44.
[16] Falat L, Schneider A, Sauthoff G, Frommeyer G. Mechanical properties of Fe–Al–M–C (M = Ti, V, Nb, Ta) alloys with strengthening carbides and laves phase. Intermetallics 2005;13:1256–62.
[17] Ohnuma I, Schön CG, Kainuma R, Inden G, Ishida K. Ordering and phase separation in the b.c.c. phase of the Fe–Al–Ti system. Acta Mater 1998;46:2083–94.
[18] Zhao PZ, Kozakai T, Miyazaki T. Phase separations into A2+ DO3 two phases in Fe–Al–V ternary ordering alloys. J Jpn Inst Met 1989;53:266–72.
[19] Morris DG, Requejo LM, Muñoz-Morris MA. Age hardening in some Fe–Al–Nb alloys. Scr Mater 2006;54:393–7.
[20] Hanus P, Bartsch E, Palm M, Krein R, Bauer-Partenheimer K, Janschek P. Mechanical properties of a forged Fe–25Al–2Ta steam turbin blade. Intermetallics 2010;18:1379–84.
[21] Witusiewicz VT, Bondar AA, Hecht U, Voblikov VM, Tsyganenko NI, Fomichov OS, et al. Experimental study and thermodynamic modeling of the ternary Al–Fe–Ta system. J Mater Sci 2013;48:377–412.
[22] Palm M, Lacaze J. Assessment of the Al–Fe-Ti system. Intermetallics 2006;14:1291–303.
[23] Gupta KP, Rajan NS, Beck PA. Effect of Si and Al on the stability of certain sigma phases. Trans AIME 1960;218:617–24.
[24] Maebashi T, Kozakai T, Doi M. Phase equilibria in iron-rich Fe–Al–V ternary alloy system. Z Metallkde 2004;95:1005–10.
[25] Krein R, Palm M, Heilmaier M. Characterization of microstructures, mechanical properties, and oxidation behavior of coherent A2 + $L2_1$ Fe–Al–Ti. J Mater Res 2009;24:3412–21.
[26] Herrmann J, Inden G, Sauthoff G. Deformation behaviour of iron-rich iron-aluminium alloys at high temperatures. Acta Mater 2003;51:3233–42.
[27] Rack HJ. The influence of titanium additions on the fracture behavior of iron. Met Trans 1972;3:1667–70.
[28] Jellison JL, Stoloff NS. Plastic deformation and fracture of Fe-V alloys. Mater Sci Eng 1974;13:231–43.
[29] Risanti D, Deges J, Falat L, Kobayashi S, Konrad J, Palm M, et al. Dependence of the brittle-to-ductile transition temperature (BDTT) on the Al content of Fe–Al alloys. Intermetallics 2005;13:1337–42.

[30] Palm M, Sauthoff G. Deformation behaviour and oxidation resistance of single-phase and two-phase L21-ordered Fe–Al–Ti alloys. Intermetallics 2004;12:1345–59.
[31] Nishino Y, Makino Y. Effect of vanadium substitution on strength properties of Fe_3Al-based alloys. Mater Sci Eng A 2001;319–321:368–71.
[32] Stein F, Schneider A, Frommeyer G. Flow stress anomaly and order–disorder transitions in Fe_3Al-based Fe–Al–Ti–X alloys with X = V, Cr, Nb, or Mo. Intermetallics 2003;11:71–82.
[33] Alonso PR, Gargano PH, Bozzano PB, Ramírez-Caballero GE, Balbuena PB, Rubiolo GH. Combined ab initio and experimental study of A2 + L21 coherent equilibria in the Fe–Al–X (X = Ti, Nb, V) systems. Intermetallics 2011;19:1157–67.
[34] Van de Walle A, Ghosh G, Asta M. Ab initio modeling of alloy phase equilibria. In: Bozzolo G, Noebe RD, Abel PB, editors. Applied computational materials modeling. Heidelberg (Germany): Springer; 2007. pp. 1–28.
[35] Smith E, Nutting J. Direct carbón replica from metal surfaces. Brit J Appl Phys 1956;7:214–7.
[36] Marcinkowski MJ, Brown N. Theory and direct observation of dislocations in the Fe_3Al superlattices. Acta Metall 1961;9:764–86.
[37] Kelly PM, Jostsons A, Blake RG, Napier JG. The determination of foil thickness by scanning transmission electron microscopy. Phys Stat Sol A 1975;31:771–80.
[38] Hattestrand M, Andren H. Evaluation of particle size distributions of precipitates in a 9% chromium steel using energy filtered transmission electron microscopy. Micron 2001;32:789–97.
[39] Whitmorea L, Leitnera H, Povoden-Karadenizb E, Radisb R, Stockingerd M. Transmission electron microscopy of single and double aged 718Plus superalloy. Mater Sci Eng A 2012;534:413–23.
[40] Batte AD, Honeycombe RWK. Strengthening of ferrite by vanadium carbide precipitation. Metal Sci J 1973;7:160–8.
[41] Tekin E, Kelly PM. Secondary hardening of vanadium steels. J Iron Steel Inst 1965;203:715–20.
[42] Batte AD, Honeycombe RWK. Precipitation of vanadium carbide in ferrite. J Iron Steel Inst 1973;211:284–9.
[43] Kainuma R, Ohnuma I, Ishida K. Determination of phase diagrams involving order–disorder transitions. In: Zhao JC, editor. Methods for phase diagram determination. New York: Elsevier; 2007. pp. 361–82.
[44] Allen SM, Cahn JW. Mechanisms of phase transformations within the miscibility gap of Fe-rich Fe-Al alloys. Acta Metall 1976;24:425–37.
[45] Chevalier JP, Stobbs WM. The state of local order in quenched CuPt. Acta Metall 1979;27:285–9.
[46] Labusch R. Statistical theories of solid solution hardening. Acta Metall 1972;20:917–27.
[47] Stoloff NS, Davies RG. The mechanical properties of ordered alloys. Prog Mater Sci 1968;13:1–84.
[48] Davies RG, Stoloff NS. Mechanical properties and superlattice formation of Mg_3Cd. Trans AIME 1964;230:390–5.
[49] Flinn PA. Solute hardening of close-packed solid solutions. Acta Metall 1958;6:631–5.
[50] Brailsford AD, Wynblatt P. The dependence of Ostwald ripening kinetics on particle volume fraction. Acta Metall 1979;21:489–97.
[51] Taillard R, Pineau A. Room temperature tensile properties of Fe-19 wt.%Cr alloys precipitation hardened by the intermetallic compound NiAl. Mater Sci Eng 1982;56:219–31.
[52] Edahiro T, Kouzai K, Yasuda HY. Mechanical properties and hardening mechanism of Fe–Al–Ni single crystals containing NiAl precipitates. Acta Mater 2013;61:1716–25.
[53] Brown LM, Ham RK. Dislocation particle interactions. In: Kelly A, Nicholson RB, editors. Strengthening methods in crystals. Amsterdam: Elsevier; 1971. pp. 10–136.
[54] Reppich B. Particle strengthening. In: Mughrabi H, editor. Materials science and technology, plastic deformation and fracture of materials. Weinheim: Wiley-VCH; 1992. p. 312.
[55] Nembach E. Precipitation hardening caused by a difference in shear modulus between particle and matrix. Phys Stat Sol A 1983;78:571–81.
[56] Buckley RA, Kaviani S. Some aspects of rapid solidification processing of Fe–Al–X alloys. Mater Sci Eng 1998;A258:173–80.
[57] Köster W, Gödecke T. Physical measurements on iron-aluminum alloys between 10 and 50 at.% Al. IV: the modulus of elasticity of the alloys. Z Metallkde 1982;73:111–4.
[58] Nishino Y, Kato M, Asano S, Soda K, Hayasaki M, Mizutani U. Semiconductorlike behavior of electrical resistivity in Heusler-type Fe_2VAl compound. Phys Rev Lett 1997;79:1909–12.
[59] Sharma V, Pilania G. Electronic, magnetic, optical and elastic properties of Fe_2YAl(Y = Ti, V and Cr) using first principles methods. J Magn Magn Mater 2013;339:142–50.
[60] Eleno LTF, Errico LA, Gonzales-Ormeño PG, Petrilli HM, Schön CG. Ordering phase relationships in ternary iron aluminides. Calphad. http://dx.doi.org/10.1016/j.calphad.2013.06.009; 2013.
[61] Reppich B. Strengthening mechanisms in MgO containing coherent stress-free precipitation particles-I. theory. Acta Metall 1976;23:1055–60.
[62] Ashby MF. The theory of the critical shear. In: Ansell GS, Cooper TD, Lenel FV, editors. Oxide dispersion strengthening. New York: Gordon & Breach; 1968. pp. 143–205.